A MEMS-Based Fast-Response Miniature Five-Hole Probe With Optical Pressure Transducers

Haocheng Zhou and Mark Sheplak, *Member, IEEE*

***Abstract*— This paper presents the first realization of a fiber-optic lever-based, miniature five-hole probe (5HP) for aerodynamic flow angle sensing applications. Five MEMS optical transducers are embedded in a hemispheric probe tip to mitigate the pneumatic lag problem of conventional 5HP technology. A silicon die with five optical pressure transducers of 400 μm radius is microfabricated from a silicon-on-insulator (SOI) wafer and bonded to a hemispheric tip of 5 mm diameter. The optimal transducer and probe tip designs are determined using lumped element modeling. Laser micromachining is utilized to drill micro holes of about 50 μm radius on the hemispheric tip. The optical transduction allows for remotely located electronics. This facilitates probe miniaturization and offers potential for high-temperature capability. The resulting 5HP has a fast response with a modeled settling time of 0.24 ms and a measured high-frequency range of about 3.5 kHz. [2020-0182]**

***Index Terms*— Fast-response, fiber-optic lever, five-hole probe (5HP), microelectromechanical systems (MEMS), pressure transducer.**

I. Introduction

TIME-EFFICIENT fluid flow velocity and pressure measurements are crucial in expensive commercial wind tunnels [1]. A 5HP is an intrusive sensor that provides point measurements in flow fields, yielding velocity vectors and pressures [2]. Compared to other flow instrumentation, a 5HP is robust and applies to both laboratory facilities and flight tests [3].

Traditional 5HPs have insufficient bandwidth, long response times, and low productivity in wind tunnel tests due to pneumatic lag induced by the tubes that transmit pressure from the tip pressure ports to the remote pressure sensors [1]. To reduce the pneumatic tube distance, several research groups installed commercial pressure transducers into the probe [4]–[7]. However, due to their relatively large size, the commercial pressure transducers are usually embedded in the probe shaft at a distance from the probe tip. This approach fails to fully solve the pneumatic lag problem as the probe still possesses a reduced pneumatic tube length. For example, Naughton *et al.* [4] developed a fast response cone-tip 5HP by embedding commercial piezoresistive transducers from Endevco Corporation in the probe shaft. The remaining pneumatic tube length is about 65 mm, which resulted in a settling time of about 20 ms.

Ned *et al.* flush-mounted five piezoresistive transducers at the probe tip surface [8]. The pneumatic tubing was eliminated by this approach. Unfortunately, the piezoresistive transducers used reportedly had a heat generation of about 0.1 watts each, which resulted in a dissipation power density of about 0.79 watt/cm^2 for the 6.35 mm diameter probe tip. This is a perturbing heat source that can alter the flow field and may cause unreliable measurements.

This effort addresses the need for reduced lag times by bonding a MEMS die with five optical pressure transducers to a laser-micromachined Pyrex hemispheric tip such that the pressure measurements occur right at the probe tip. The fiber-optic lever, shown in Fig. 1, is the transduction mechanism in this project. It is a light intensity modulation based on the optical path distance and has been widely exploited in displacement sensing [9]–[12]. This transduction scheme only requires optical fibers to be embedded in the probe tip. It enables probe miniaturization and possesses no heat generation as opposed to the piezoresistive method in Ned *et al.* [8].

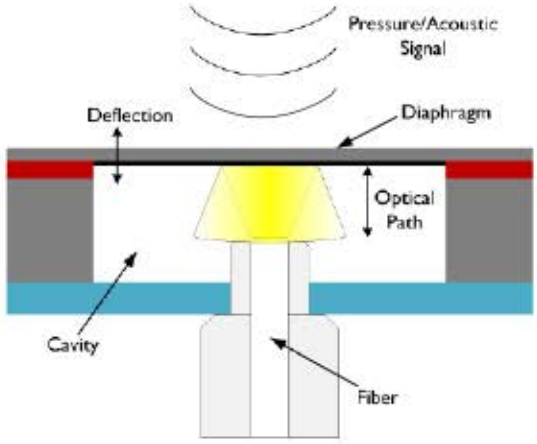

Fig. 1. A schematic illustrating the transduction mechanism for a fiber-optic lever pressure sensor.

II. Design

A. Structure

The optical MEMS 5HP structure, shown in Fig. 2, includes a MEMS die, a hemispheric tip, and a multi-fiber ferrule.

Manuscript received May 15, 2020; revised June 30, 2020; accepted July 6, 2020. Date of publication July 27, 2020; date of current version October 7, 2020. This work was supported in part by the NSF I/UCRC on Multi-functional Integrated System Technology (MIST) Center under Grant IIP-1439644, Grant IIP-1439680, and Grant IIP-1738752. Subject Editor M. Rais-Zadeh. *(Corresponding author: Haocheng Zhou.)*

The authors are with the Interdisciplinary Microsystems Group, Department of Mechanical and Aerospace Engineering, University of Florida, Gainesville, FL 32611 USA (e-mail: haochengzhou@outlook.com; sheplak@ufl.edu).

Color versions of one or more of the figures in this letter are available online at http://ieeexplore.ieee.org.

Digital Object Identifier 10.1109/JMEMS.2020.3009927

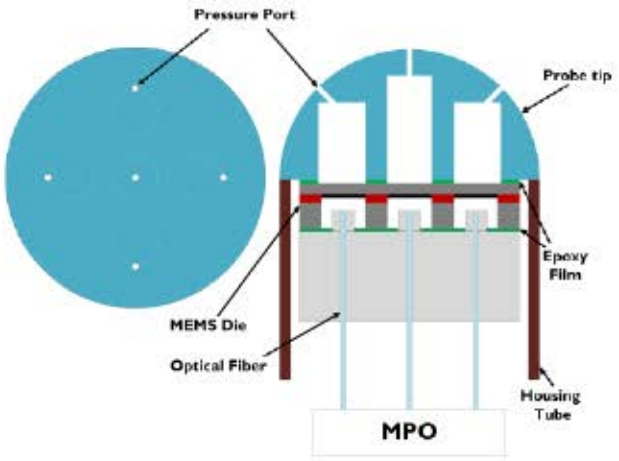

Fig. 2. Optical MEMS 5HP structure.

The MEMS die has an array of five transducer diaphragms that deflect linearly with pressure inputs. The hemispheric tip includes five Helmholtz resonators that transmit the probe tip surface pressures to the diaphragms. The multi-fiber ferrule holds five multi-mode optical fibers that send light to and receive light from the diaphragm.

B. Modeling and Optimization

Lumped element modeling is utilized for designing the pressure transducers and the Helmholtz resonators. Because the Helmholtz resonator cavity compliance is much greater than the transducer diaphragm compliance, the coupling between the two oscillators is weak. As a result, the performances of the transducers and Helmholtz resonators are essentially unaffected by each other and their modeling and optimization are conducted separately. The design goal for the transducers is to achieve the lowest minimum detectable pressure (MDP), given constraints on geometry, dynamic range, and resonant frequency. The design goal for the Helmholtz resonators is to achieve minimum and equal settling times for the central and peripheral Helmholtz resonators, given constraints on geometric and fabrication limitations. The MATLAB fmincon solver is used for both optimization processes. Lumped element modeling predicted a settling time of about 0.24 ms for the optimal design. This settling time is about two orders of magnitude faster than the example in Naughton *et al.* [4].

For a fiber optic lever, the optical sensitivity is independent of the mechanical sensitivity [9]. To achieve the maximum optical sensitivity, a fiber-optic lever characterization on an optical table is conducted to find the optimal fiber-mirror distance. The fiber and a reflective mirror are moved apart from contact using a nano-positioner, as shown in Fig. 3(a), and the experimental results are shown in Fig. 3(b). A Doric LEDP1 narrow-band light source with a central wavelength of 850 nm is used. To compensate for LED source drift, the voltage output of the reflected light intensity, Vs, is normalized by the voltage output of a reference channel light intensity, Vr. The optimal fiber-mirror distance is located at the maximum slope region of the curve in Fig. 3(b), which is found to be between 20 μm to 50 μm.

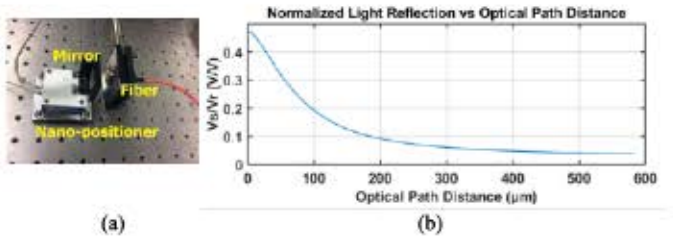

Fig. 3. Fiber-optic lever characterization. (a) Optical table experimental setup. (b) Optical table experimental results.

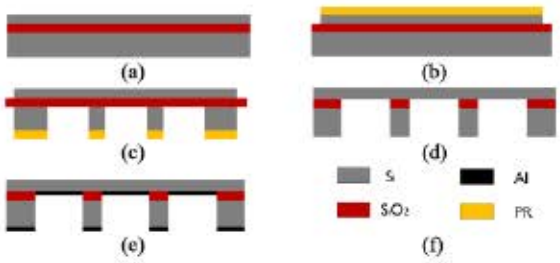

Fig. 4. Fabrication of MEMS 5HP die from SOI wafer. (a) SOI wafer. (b) Frontside photolithography. (c) Backside photolithography. (d) Buried oxide etching. (e) Sputtering of aluminium layer. (f) Color of materials.

III. Fabrication

The fabrication of the MEMS die begins with an SOI wafer with a 5.5 μm thick device layer, a 600 μm thick handle layer, and a 1 μm thick buried oxide layer [Fig. 4(a)]. Frontside processing [Fig. 4(b)] involves a photolithography step and a deep-reactive ion etching (DRIE) step that patterns the circular die edge and four rectangular marks for alignment during packaging. Backside processing [Fig. 4(c)] involves a front-to-back alignment for photolithography and a DRIE step to create five circular cavities, resulting in five diaphragms of 800 μm diameter. A hydrofluoric vapor etching step follows to remove the exposed buried oxide layer and achieve die separation [Fig. 4(d)]. A 150 nm thick aluminium layer is then deposited via sputtering on the backside of the diaphragm as a light-reflective layer [Fig. 4(e)].

The fabrication of the hemispheric tip starts with Pyrex spheres of 5 mm diameter purchased from Thorlabs, Inc. The Pyrex spheres are ground into hemispheres and Helmholtz resonator cavities are drilled by vendor Insaco, Inc. The machining of the pressure holes on the tip surface is accomplished by a 355 nm Oxford laser micromachining station that uses ultrashort laser pulses for material ablation [13]. The laser beam has a spot size of 9 μm, enabling the drilling of hole diameters on the order of 100 μm, shown in Fig. 5. The small hole size provides high spatial resolution for pressure measurements. It also reduces the possibility of the holes being covered by flow separation at high flow incident angles, extending the angular range of the 5HP.

The multi-fiber ferrule uses a stainless-steel housing to fit five zirconia ferrules of 1.25 mm diameter, shown in Fig. 6(a). Each ferrule has a laser-micromachined step column, and the step heights are used to achieve the optimal fiber-mirror distance. A scanning white light interferometry (SWLI) topography test is conducted to verify the ferrule step heights and

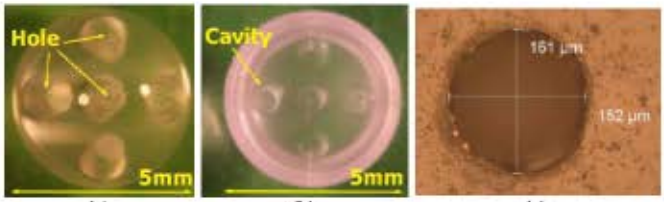

Fig. 5. Pyrex hemispheric tip. (a) Pressure holes on the frontside. (b) Cavities on the backside. (c) Laser-micromachined pressure hole.

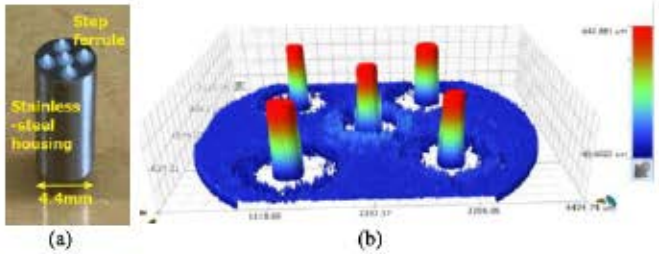

Fig. 6. Multi-fiber ferrule and SWLI topography test. (a) Step ferrules fitted in a stainless-steel housing. (b) SWLI test results.

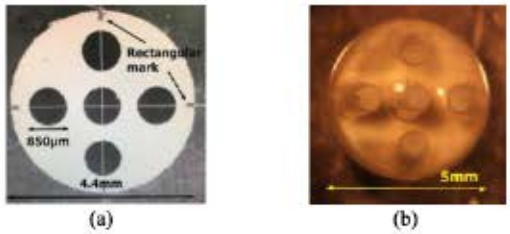

Fig. 7. Tip to die bonding. (a) Laser-patterned epoxy film. (b) Bonded piece.

the results are shown in Fig. 6(b). The measured step heights are 640 μm, 583 μm, 614 μm, 628 μm, and 610 μm.

IV. Packaging

The packaging process is comprised of three main steps: the bonding of the hemispheric tip to the silicon die, the bonding of the multi-fiber ferrule to the die, and the termination of the optical fibers.

The bonding of the tip to the die is accomplished using a LOCTITE Ablestik 561K epoxy film of 125 μm thickness. To match the tip and die geometry, the epoxy film is first patterned using laser micromachining, shown in Fig. 7(a). The patterning includes the die edge, five diaphragms, and four rectangular marks around the edge to align with the same marks on the frontside of the die. The bonding is carried out on a flip-chip bonder that provides alignment, bonding pressure, and high temperature of 150 °C for epoxy curing. The bonded piece is shown in Fig. 7(b).

The bonding of the multi-fiber ferrule to the die also uses the same laser-patterned epoxy film. Multi-mode fibers are first fixed into the ferrules using fiber epoxy and polished. During bonding, the multi-fiber ferrule is clamped to the flip-chip bonder using a setscrew hole. A stainless-steel tube of 5 mm diameter and 250 μm wall thickness is glued to the probe tip as the protective probe tube. Finally, a multi-fiber push-on (MPO) connector is used to terminate the fibers so that the

Fig. 8. Fully packaged optical MEMS 5HP.

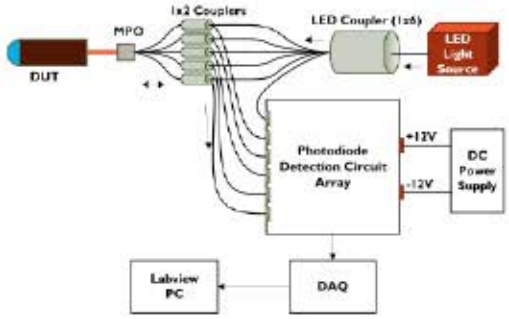

Fig. 9. Optoelectronic system for the optical MEMS 5HP.

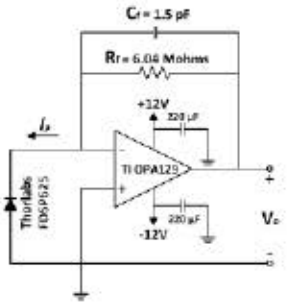

Fig. 10. Photodiode detection circuit design.

5HP can be connected to the optoelectronic system. The packaged optical MEMS 5HP is shown in Fig. 8.

V. Optoelectronic System

The 5HP optoelectronic system is shown in Fig. 9. A custom-designed 1 × 6 optical coupler, manufactured by Timbercon, Inc., is used to split the LED light into six channels, one of which is a reference. The other five channels are each connected to a 1 × 2 coupler before light is sent to the MEMS transducers. A photodiode detection circuit array is designed and fabricated to measure the light intensity and to output voltage signals. Output normalization by the reference channel is utilized to mitigate the light intensity drift of the LED.

The photodiode detection circuit, shown in Fig. 10, is comprised of a photodiode that generates a photocurrent based on the light intensity, and a transimpedance amplifier that amplifies the photocurrent into a voltage signal. The photodiode used is a Thorlabs FDSP625 pigtailed photodiode and the transimpedance amplifier uses a Texas Instruments OPA 129 op-amp with a feedback resistor of 6.04 MΩ and a feedback capacitor of 1.5 pF.

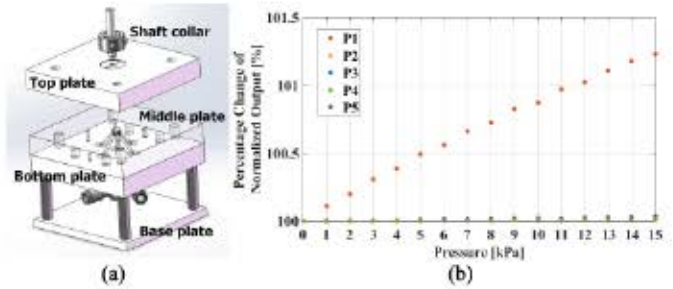

(a) (b)

Fig. 11. 5HP sealing test. (a) Sealing test experimental setup. (b) Central pressure channel (P1) sealing test results.

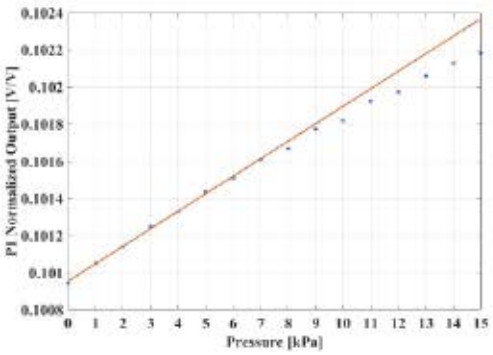

Fig. 12. 5HP central pressure channel (P1) static calibration results.

VI. Experimental Setups and Results

A. Sealing Test and Static Calibration

Each transducer is expected to measure a pressure at a different location on the probe tip. Crosstalk between channels due to leakage would render the pressure measurements unreliable. A seal test is conducted to prove that each individual pressure channel is sealed from the others and the atmosphere. The seal test setup, shown in Fig. 11(a), uses a hemispheric recess and micro O-rings of 1.88 mm diameter to apply pressure inputs to only one port with a Fluke 718 30G pressure calibrator. The sealing test results for the central port (port 1), as an example, are shown in Fig. 11(b). When pressure is applied to port 1, only P1 exhibits a stable and linear response, proving that port 1 is sealed from other ports and the atmosphere.

The same setup is also used for the static calibration of the individual pressure channels. As an example, Fig. 12 shows a least-squares linear curve fit from 0 kPa to 8 kPa for the central port, where the voltage output normalized by the LED reference is plotted against the static pressure. The output error bar is calculated as the random error of the mean using a 95% confidence interval and the pressure error bar is the uncertainty level provided by the pressure calibrator manufacturer. A Monte Carlo simulation is then conducted to determine the distribution and uncertainty of the estimated sensitivity [14]. Random perturbations are applied before the curve fit to both the output mean and the pressure based on their own distributions, and 10,000 iterations are conducted. The probability density function (PDF) of the normalized sensitivity with a Gaussian distribution fit is shown in Fig. 13(a).

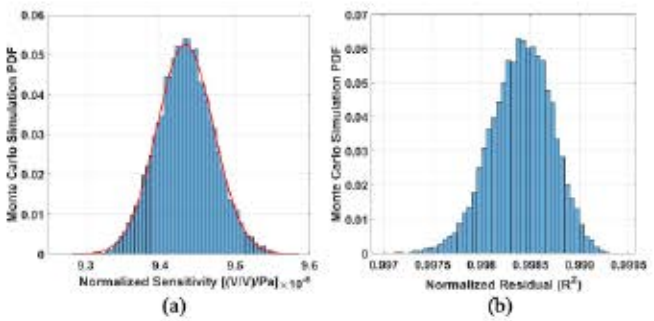

(a) (b)

Fig. 13. Central pressure channel (P1) static calibration Monte Carlo simulation results. (a) PDF of normalized sensitivity. (b) PDF of normalized residual.

TABLE I
Pressure Channels Static Calibration Results

Port #	Sensitivity Mean $\times 10^{-8}$ (V/V)/Pa	Sensitivity Uncertainty $\times 10^{-8}$ (V/V)/Pa	3% Nonlinearity Pressure Load kPa
P1	9.43	0.04	8.0
P2	17.36	0.07	9.0
P3	18.35	0.09	9.0
P4	9.51	0.04	8.0
P5	32.03	0.13	9.0

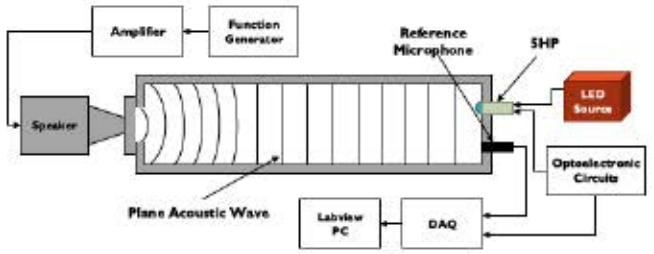

Fig. 14. PWT setup for the dynamic calibration of pressure channels.

The normalized residual of the linear curve fit is shown in Fig. 13(b). The 3% nonlinearity pressure load of each transducer was determined via the static pressure calibration, shown in Fig 12. The static calibration results for all five pressure ports are shown in Table I.

B. Dynamic Calibration

The dynamic calibration, shown in Fig. 14, is conducted in a plane wave tube (PWT) to determine the frequency response of the pressure channels [15]. Only plane wave propagation is permitted when acoustic waves are generated by a speaker into the PWT below its cut-off frequency of 6.7 kHz [16]. The lower frequency limit is 300 Hz due to the inefficiency of the speaker at low frequencies. The 5HP is mounted adjacent to a Bruel and Kjaer 1/8-inch reference microphone at the PWT rigid end wall which is a sound hard boundary. An Agilent 33220A function generator and a National Instruments PXI data acquisition system are used to tune the acoustic wave magnitude and frequency. The sampling rate of the dynamic calibration is 20 kHz. The number of ensemble averages is 100 with 2000 samples per block.

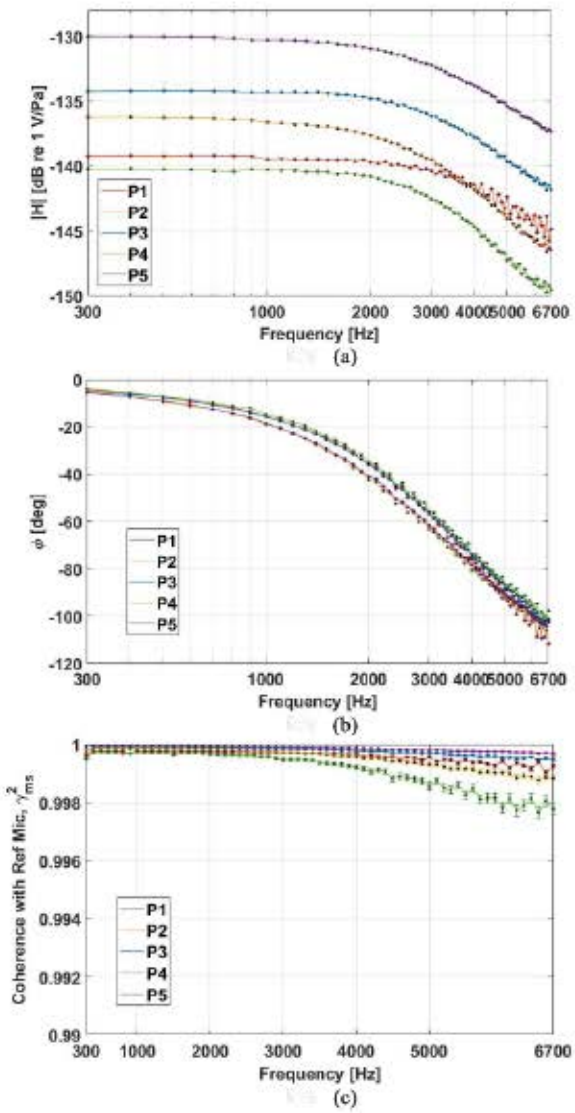

Fig. 15. 5HP dynamic calibration results. (a) FRF magnitude. (b) FRF phase. (c) FRF coherence.

The dynamic calibration results, including the frequency response magnitude, phase, and the coherence between the pressure channels and the reference microphone, are shown in Fig. 15. The frequency magnitudes of the pressure channels exhibit a flatband from the low frequency limit until the roll off effect of the Helmholtz resonators occurs. High coherence (>0.997) is found for all channels across the test frequency range. The ±3dB bandwidth of the five pressure channels, from port 1 to port 5, are 4.5 kHz, 3.0 kHz, 3.7 kHz, 3.4 kHz, 3.6 kHz, respectively.

C. Noise and MDP

The noise floor is measured with no pressure input applied to the 5HP. The sampling rate of the noise characterization is 20 kHz. The number of ensemble averages is 1000 with 2000 samples per block and the frequency resolution is 10 Hz. A Hanning window with 75% overlap is applied to the spectral estimation to mitigate spectral leakage.

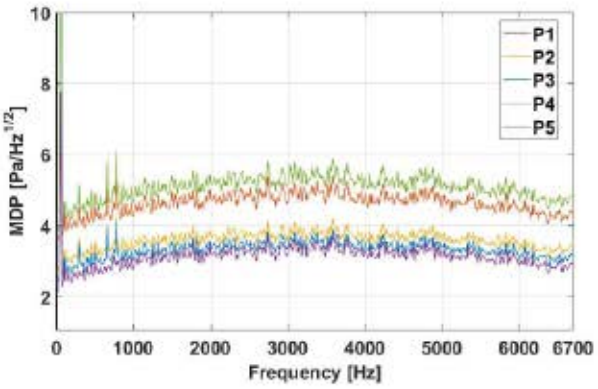

Fig. 16. 5HP MDPs from noise floor measurements.

The noise spectra of the five pressure channels are divided by their respective sensitivities to calculate the MDP of each channel. Fig. 16 shows the MDP of the five pressure channels based on their noise floor measurements. The noise floor is flat across the whole frequency range, as the dominant noise source of the optical transducers is the frequency-independent shot noise of the photodiode in the optoelectronic system. The MDPs of the five pressure channels at 1 kHz, from port 1 to port 5, are 3.06 Pa, 4.28 Pa, 3.32 Pa, 2.83 Pa, 4.69 Pa, respectively.

VII. Conclusion

This study focused on the development of a fiber-optic lever-based MEMS 5HP with a fast response and a high bandwidth. The realized 5HP has a predicted settling time of only 0.24 ms, mainly intended to reduce experimental time in commercial flow facilities. The low settling time can greatly reduce operational and labor cost in wind tunnel tests and allows fast in situ aircraft measurements with minimal time delay. Microfabrication and laser micromachining are utilized for the fabrication of the MEMS 5HP. A sealing test proved no leakage between the five pressure channels of the packaged 5HP. The static and dynamic calibrations of the pressure channels showed bandwidths from 3 kHz to 4.5 kHz and MDPs from 2.83 Pa to 4.69 Pa. Future work will focus on assessing the thermal and vibrational stability of the pressure measurements, and the wind tunnel characterization of the 5HP as a whole system.

References

[1] J. Crowder *et al.*, "Airplane flow-field measurements," in *Proc. World Aviation Congr.*, Anaheim, CA, USA, 1997, p. 5535.

[2] C. Tropea, A. Yarin, and J. F. Foss, "Velocity, vorticity, and mach number," in *Springer Handbook of Experimental Fluid Mechanics*, vol. 1, 1st ed. Berlin, Germany: Springer-Verlag, 2007, pp. 216–228, ch. 5, sec. 5.

[3] D. Telionis, Y. Yang, and O. Rediniotis, "Recent developments in multi-hole probe (MHP) technology," in *Proc. COBEM*, Gramado, RS, Brazil, 2009, p. 21.

[4] J. Naughton, L. Cattafesta, and G. Settles, "A miniature fast-response five-hole probe for supersonic flowfield measurements," *AIAA J.*, vol. 31, no. 3, pp. 453–458, Mar. 1993.

[5] R. W. Ainsworth, J. L. Allen, and J. J. M. Batt, "The development of fast response aerodynamic probes for flow measurements in turbomachinery," *J. Turbomach.*, vol. 117, no. 4, pp. 625–634, Oct. 1995.

[6] P. Kupferschmied *et al.*, "Time-resolved flow measurements with fast-response aerodynamic probes in turbomachines," *Meas. Sci. Technol.*, vol. 11, no. 7, p. 1036, Jul. 2000.
[7] D. P. Georgiou and K. F. Milidonis, "Fabrication and calibration of a sub-miniature 5-hole probe with embedded pressure sensors for use in extremely confined and complex flow areas in turbomachinery research facilities," *Flow Meas. Instrum.*, vol. 39, pp. 54–63, Oct. 2014.
[8] A. A. Ned *et al.*, "High Accuracy, High Temperature Pressure Probes for Aerodynamic Testing," in *Proc. 49th AIAA Aerosp. Sci. Meet.*, Orlando, FL, USA, 2011, p. 1021.
[9] G. He and F. W. Cuomo, "A light intensity function suitable for multi-mode fiber-optic sensors," *J. Lightw. Technol.*, vol. 9, no. 4, pp. 545–551, Apr. 1991.
[10] Z. Gong, K. Chen, Y. Yang, X. Zhou, W. Peng, and Q. Yu, "High-sensitivity fiber-optic acoustic sensor for photoacoustic spectroscopy based traces gas detection," *Sens. Actuators B, Chem.*, vol. 247, pp. 290–295, Aug. 2017.
[11] T. Lan, C. Zhang, S. Fu, B. Zhu, M. Tang, and W. Tong, "Spatial division multiplexing-based reflective intensity-modulated fiber optics displacement sensor," *IEEE Photon. J.*, vol. 10, no. 4, Aug. 2018, Art. no. 7103707.
[12] H. Zhou, D. A. Mills, A. Vera, A. Garraud, W. Oates, and M. Sheplak, "A high-temperature optical sapphire pressure sensor for harsh environments," in *Proc. AIAA Scitech Forum*, Jan. 2019, p. 2044.
[13] P. Woerner, D. Blood, D. Mills, M. Sheplak, and W. S. Oates, "Quantifying the uncertainty of picosecond pulsed laser ablation in sapphire," *J. Manuf. Processes*, vol. 35, pp. 687–699, Oct. 2018.
[14] V. Chandrasekharan, J. Sells, J. Meloy, D. P. Arnold, and M. Sheplak, "A microscale differential capacitive direct wall-shear-stress sensor," *J. Microelectromech. Syst.*, vol. 20, no. 3, pp. 622–635, Jun. 2011.
[15] T. Schultz, L. N. Cattafesta, and M. Sheplak, "Modal decomposition method for acoustic impedance testing in square ducts," *J. Acoust. Soc. Amer.*, vol. 120, no. 6, pp. 3750–3758, Dec. 2006.
[16] M. D. Williams, B. A. Griffin, T. N. Reagan, J. R. Underbrink, and M. Sheplak, "An AlN MEMS piezoelectric microphone for aeroacoustic applications," *J. Microelectromech. Syst.*, vol. 21, no. 2, pp. 270–283, Apr. 2012.

Haocheng Zhou received the B.S. degree in thermal science and power engineering from North China Electric Power University, Beijing, China, in 2014, and the M.S. degree in mechanical engineering and the M.S. degree in electrical and computer engineering from the University of Florida (UF), Gainesville, FL, in 2016 and 2018, respectively, where he is currently pursuing the Ph.D. degree in mechanical engineering.

His work focuses on the development and characterization of microelectromechanical-systems-based transducers.

Mark Sheplak (Member, IEEE) received the B.S., M.S., and Ph.D. degrees in mechanical engineering from Syracuse University, Syracuse, NY, USA, in 1989, 1992, and 1995, respectively.

He is currently a Professor holding joint appointments with the Department of Mechanical and Aerospace Engineering and the Department of Electrical and Computer Engineering, University of Florida (UF). Prior to joining UF in 1998, he was a Postdoctoral Associate with the Microsystems Technology Laboratories, Massachusetts Institute of Technology, Cambridge, MA, USA, from 1995 to 1998. His current research focuses on the design, fabrication, and characterization of high-performance, instrumentation-grade, MEMS-based sensors and actuators that enable the measurement, modeling, and control of various physical properties. He is a member of the Multi-Functional Integrated System Technology Center and the Florida Center for Advanced Aero-Propulsion. He is an Associate Fellow of AIAA and a fellow of the Acoustical Society of America.